



CrossMark
click for updates

Cite this: *J. Mater. Chem. A*, 2015, 3, 207

Vertically aligned nanocomposite $\text{La}_{0.8}\text{Sr}_{0.2}\text{CoO}_3/(\text{La}_{0.5}\text{Sr}_{0.5})_2\text{CoO}_4$ cathodes – electronic structure, surface chemistry and oxygen reduction kinetics†

Wen Ma,^a Jae Jin Kim,^b Nikolai Tsvetkov,^a Takeshi Daio,^c Yener Kuru,^{ab} Zhuhua Cai,^a Yan Chen,^a Kazunari Sasaki,^c Harry L. Tuller^b and Bilge Yildiz^{*a}

The hetero-interfaces between the perovskite $(\text{La}_{1-x}\text{Sr}_x)\text{CoO}_3$ (LSC_{113}) and the Ruddlesden-Popper $(\text{La}_{1-x}\text{Sr}_x)_2\text{CoO}_4$ (LSC_{214}) phases have recently been reported to exhibit fast oxygen exchange kinetics. Vertically aligned nanocomposite (VAN) structures offer the potential for embedding a high density of such special interfaces in the cathode of a solid oxide fuel cell in a controllable and optimized manner. In this work, VAN thin films with hetero-epitaxial interfaces between LSC_{113} and LSC_{214} were prepared by pulsed laser deposition. *In situ* scanning tunneling spectroscopy established that the LSC_{214} domains in the VAN structure became electronically activated, by charge transfer across interfaces with adjacent LSC_{113} domains above 250 °C in 10^{-3} mbar of oxygen gas. Atomic force microscopy and X-ray photoelectron spectroscopy analysis revealed that interfacing LSC_{214} with LSC_{113} also provides for a more stable cation chemistry at the surface of LSC_{214} within the VAN structure, as compared to single phase LSC_{214} films. Oxygen reduction kinetics on the VAN cathode was found to exhibit approximately a 10-fold enhancement compared to either single phase LSC_{113} and LSC_{214} in the temperature range of 320–400 °C. The higher reactivity of the VAN surface to the oxygen reduction reaction is attributed to enhanced electron availability for charge transfer and the suppression of detrimental cation segregation. The instability of the $\text{LSC}_{113/214}$ hetero-structure surface chemistry at temperatures above 400 °C, however, was found to lead to degraded ORR kinetics. Thus, while VAN structures hold great promise for offering highly ORR reactive electrodes, efforts towards the identification of more stable hetero-structure compositions for high temperature functionality are warranted.

Received 21st September 2014
Accepted 15th October 2014

DOI: 10.1039/c4ta04993d

www.rsc.org/MaterialsA

1. Introduction

Solid oxide fuel cells (SOFCs) have high energy conversion efficiencies and lower emissions than combustion systems by virtue of their ability to directly convert the chemical energy stored in fuels into electrical energy at elevated temperatures.¹ To render them economically feasible, functionality at intermediate temperatures (500–700 °C), and at even lower temperatures (350–500 °C) for microdevices, is desirable, thereby lowering the cost and increasing the lifetime of SOFC systems.^{2–8} At these reduced temperatures, however, the performance of the cathode becomes a challenge, due to the sluggish kinetics of the oxygen reduction reaction on

traditionally used cathode materials. The cathode effectively catalyzes the oxygen reduction by providing available sites^{9,10} for oxygen adsorption and by transferring electrons from the solid to the adsorbing oxygen in a facile manner.^{4,11,12}

There has been several recent reports showing that interfaces between the perovskite $(\text{La}_{1-x}\text{Sr}_x)\text{CoO}_3$ (LSC_{113}) and the Ruddlesden-Popper $(\text{La}_{1-x}\text{Sr}_x)_2\text{CoO}_4$ (LSC_{214}) phases in the $\text{LSC}_{113/214}$ hetero-structure significantly facilitate oxygen reduction kinetics.^{13–17} Sase *et al.*^{14,15} showed that the oxygen exchange kinetics near these dissimilar interfaces is increased by three to four orders of magnitude with respect to single phase LSC_{113} or LSC_{214} at 500 °C. Such an astonishing improvement of oxygen exchange kinetics was also confirmed by electrochemical measurements at 550 °C and 600 °C.^{16,17} In order to go beyond this isolated example and design active and stable hetero-interfaces for accelerating ORR in a controllable way on oxide surfaces, a microscopic level understanding of the mechanisms behind such an unusual enhancement is needed. For this purpose, we recently reported on the electronic structure at the surface of $\text{LSC}_{113/214}$ hetero-structures, in the form of multilayers, by performing *in situ* scanning tunneling spectroscopy (STS) as a function of temperature and in oxygen gas.¹⁸

^aLaboratory for Electrochemical Interfaces, Department of Nuclear Science and Engineering, Massachusetts Institute of Technology, 77 Massachusetts Avenue, Cambridge, MA 02139, USA. E-mail: byildiz@mit.edu

^bDepartment of Materials Science and Engineering, Massachusetts Institute of Technology, 77 Massachusetts Avenue, Cambridge, MA 02139, USA

^cDepartment of Mechanical Engineering, Kyushu University, Fukuoka-shi, 819-0395 Fukuoka, Japan

† Electronic supplementary information (ESI) available. See DOI: 10.1039/c4ta04993d

The STS measurements were assisted by grazing incidence focused ion beam milling to expose the buried interfaces and layers with nm-scale resolution. Tunneling spectroscopy results revealed that the p-type LSC_{214} loses its energy gap at the surface and becomes enriched in electrons when put in contact with LSC_{113} at elevated temperatures. Considerably more electrons become available to reduce the oxygen at the LSC_{214} surface. That, combined with the preferential anisotropic oxygen incorporation into LSC_{214} (100) surfaces,¹⁹ is expected to accelerate ORR kinetics at the $\text{LSC}_{113/214}$ hetero-structures (Fig. 1a).²⁰ This finding allowed us to propose “electronically coupled oxide hetero-structures” as a new type of high-performance cathode for SOFCs.

Inspired by this model,¹⁸ the vertically aligned nanocomposite (VAN) of $\text{LSC}_{113/214}$, which benefits from the electronic activation phenomena, while maximizing the desirable active interfacial area exposed to the gas phase, is studied in this work as a new cathode structure (Fig. 1b). This serves as a more controllable alternative to the random decoration of surfaces of a phase with nano-particles of a second phase or to making a randomly mixed composite cathode.^{16,17} Vertical nanocomposite hetero-epitaxial films are of interest for various functional device applications. Fig. 1b illustrates an idealized model of such nanocomposites in which the two phases alternate in an ordered, checker-board fashion. VAN structures have been demonstrated in a number of material systems, in order to examine the tunability of electrical conductivity,²¹ dielectric loss^{22,23} and low-field magnetoresistance²³ mediated by the strain at the hetero-epitaxial interfaces. VAN oxide thin films have also stimulated interest in the field of SOFC research. Yoon *et al.*²⁴ demonstrated one to two orders of magnitude decrease of area-specific resistance of the cathode by forming a $\text{Ce}_{0.9}\text{Gd}_{0.1}\text{O}_{1.95}/\text{La}_{0.5}\text{Sr}_{0.5}\text{CoO}_3$ VAN interlayer between the cathode and the electrolyte, and this interlayer effectively increased the cathode/electrolyte interfacial contact area. The oxide ion conductivity of $(\text{Ce}_{0.9}\text{Gd}_{0.1}\text{O}_{1.95})/(\text{Zr}_{0.92}\text{Y}_{0.08}\text{O}_{1.96})$ VAN electrolyte has also been reported to be enhanced by two times

compared with YSZ or GDC thin films.²⁵ Vertically aligned nanocomposites made of different cathode materials have not been previously studied however and are examined in detail in this study of the $\text{LSC}_{113/214}$ system. Both LSC_{113} and LSC_{214} grow epitaxially on common substrates, such as SrTiO_3 (STO) and yttria stabilized zirconia (YSZ) with a gadolinium doped ceria (GDC) buffer layer.^{26–28} Given that both LSC_{113} and LSC_{214} also exhibit similar growth kinetics and that it is possible for them to phase separate in a thermodynamically stable state,^{14,17,18} the $\text{LSC}_{113/214}$ composite system offers the possibility to form high quality VAN structures.

The unique requirements needed to successfully grow and characterize the $\text{LSC}_{113/214}$ VAN structures under *in situ* conditions are described in the Experimental section below. In particular, it is worth noting that the proper synthesis conditions to form columnar growth of LSC_{113} and LSC_{214} in a phase-separated form in the VAN structure were found to reside only in a narrow temperature window, oxygen partial pressure and deposition rate during the pulsed laser deposition (See Experimental methods for details). Nano-probe Auger electron spectroscopy and *in situ* scanning tunneling microscopy were used to characterize the chemical, structural and electronic properties of the nanocomposite $\text{LSC}_{113/214}$ film with high spatial resolution. Moreover, to access the properties of these VAN structures under conditions close to the working environment of an SOFC, *in situ* scanning tunneling spectroscopy,^{18,26,29,30} with ability to operate at elevated temperatures and in oxygen gas, served to capture novel changes in the electronic structure of the VAN surface as a function of temperature.

In this work, we demonstrate the successful formation of vertically aligned nanocomposites of $\text{LSC}_{113/214}$. LSC_{113} and LSC_{214} phases form (001) orientated columnar grains with lateral dimensions in the range of 100–500 nm. Two key features, described in the Results, are the disappearance of the 0.7–1 eV energy gap at the surface of LSC_{214} when it is in the VAN structure at and above 250 °C in oxygen gas, and the improved stability of the cation composition at the surface of LSC_{214} when it is part of the VAN hetero-structure. We believe these two factors give rise to enhanced ORR kinetics, by about one order of magnitude, for $\text{LSC}_{113/214}$ VAN thin films at, or below, 400 °C, as shown by our electrochemical impedance measurements. Challenges related to long-term stability of these particular $\text{LSC}_{113/214}$ compositions used in the VAN structure at temperatures above 400 °C are also discussed.

2. Experimental methods

The $(\text{La}_{0.8}\text{Sr}_{0.2})\text{CoO}_3/(\text{La}_{0.5}\text{Sr}_{0.5})_2\text{CoO}_4$ nanocomposite film was prepared by pulsed laser deposition from a composite target onto SrTiO_3 (001) and yttria stabilized zirconia (YSZ) (001) single crystal substrates (purchased from MTI Corp). In this study, $\text{La}_{0.8}\text{Sr}_{0.2}\text{CoO}_3$ and $(\text{La}_{0.5}\text{Sr}_{0.5})_2\text{CoO}_4$ were chosen because these compositions were demonstrated by Crumlin *et al.*¹⁶ and Sase *et al.*¹⁴ to exhibit enhanced electrochemical performance with hetero-structures, albeit composed of random surface patches of LSC_{214} on LSC_{113} . For the composite target preparation, first, single-phase $(\text{La}_{0.8}\text{Sr}_{0.2})\text{CoO}_3$ and $(\text{La}_{0.5}\text{Sr}_{0.5})_2\text{CoO}_4$ powders

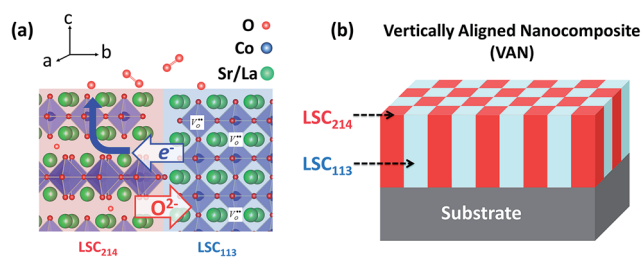


Fig. 1 (a) Schematic model of “electronically coupled oxide hetero-structures” made of LSC_{113} and LSC_{214} . At high temperature, more oxygen vacancies and free electrons are created in the LSC_{113} phase. The excess electrons are injected into LSC_{214} phase from LSC_{113} , facilitating the oxygen reduction reaction at the LSC_{214} surface. Faster ORR kinetics are expected at $\text{LSC}_{113/214}$ vertically aligned nanocomposite hetero-structures given the high density of interfaces. (Note the alignment between $\text{LSC}_{113}/\text{LSC}_{214}$ does not reflect the real geometry.) (b) Schematic checker-board illustration of a vertically aligned nanocomposite (VAN) made of LSC_{113} and LSC_{214} on a substrate.

were synthesized by the Pechini gel-type method³¹ utilizing $\text{La}(\text{NO}_3)_3 \cdot 6\text{H}_2\text{O}$, $\text{Sr}(\text{NO}_3)_2$, $\text{Co}(\text{NO}_3)_2 \cdot 6\text{H}_2\text{O}$, ethylene glycol and anhydrous citric acid as the starting materials. Aqueous solutions of the metal nitrates were mixed in the respective stoichiometric ratio by stirring, followed by addition of ethylene glycol and citric acid to form a metal-organic complex. The resultant mixtures were heated at 90 °C until a dry gel formed. After drying at 110 °C for 12 h, the as-obtained powder was pre-fired at 500 °C for 2 h and then fully calcined at 950 °C for 5 h. The phase composition of the powders was examined by X-ray diffraction ($\text{CuK}\alpha$, 45 kV and 40 mA, PANalytical X'Pert Pro Multipurpose Diffractometer, Almelo, Netherlands) at room temperature in air. In order to fabricate the composite oxide target made of $(\text{La}_{0.8}\text{Sr}_{0.2})\text{CoO}_3$ and $(\text{La}_{0.5}\text{Sr}_{0.5})_2\text{CoO}_4$, the two powders were thoroughly mixed in a 3 : 2 molar ratio. After uniaxially pressing under ~ 100 MPa for 90 seconds, the target was sintered at 1300 °C for 10 hours in air. The LSC_{113} and LSC_{214} phases remained phase separated even following sintering under these conditions as confirmed by nanoprobe Auger Electron Spectrometry measurements used to quantify the chemical composition in each phase (Table S1†). A KrF excimer laser with wavelength of 248 nm under energy constant mode (300 mJ) and pulse frequency of 2 Hz was used during deposition. Since LSC is reactive with YSZ, a 10% gadolinium doped ceria $\text{Ce}_{0.9}\text{Gd}_{0.1}\text{O}_{1.95}$ (GDC) buffer layer was deposited on the YSZ (001) substrate at 680 °C under 10 mTorr oxygen partial pressure by pulsed laser deposition in the same chamber preceding the deposition of the $\text{LSC}_{113/214}$ VAN films. The deposition conditions for the VAN film were 760 °C substrate temperature and 100 mTorr oxygen partial pressure. Following growth, the films were cooled down to room temperature in 10 Torr oxygen pressure to ensure oxidation of the films. The resulting LSC_{113} , LSC_{214} and $\text{LSC}_{113/214}$ VAN dense films of ~ 200 nm thickness were deposited either on YSZ (001) substrates coated with ~ 100 nm thick GDC buffer layers, or directly onto STO (001) substrates.

The surface cation chemistry was quantified with nm-scale spatial resolution by Scanning Nano-probe Auger Electron Spectrometry (AES) (Physical Electronics Model 700). Specifically, Co distribution was mapped to identify the phases in the VAN, and the Sr fractions in the LSC_{113} and LSC_{214} grains in the VAN were quantified and found to be similar to those in the single phase LSC_{113} and LSC_{214} films (see ESI, Table S1†). The energy and current of the incident electrons were 10 keV and 10 nA, respectively. Smoothing and differentiation of the Auger electron spectra were performed using the Savitsky-Golay algorithm. Quantification of the Auger electron differential spectra was carried out using the peak-to-peak intensities of the tight scans of the La MNN, Sr LMM, and Co LMM Auger electron emissions. The sampling depths of these Auger electrons are ~ 4 nm for La MNN, ~ 8.5 nm for Sr LMM and ~ 4.6 nm for Co LMM.³²

Cross-sectional Scanning Electron Microscopy (SEM-FEI Helios Nanolab system) was used to identify the columnar microstructure of the VAN film. The film was cut vertically with respect to the sample surface by focused Ga^+ ion-beam (FIB). In order to protect the surface features during ion milling, a $\sim 1 \mu\text{m}$

thick Pt protective cap was deposited on top by electron beam. The Ga^+ beam current and acceleration voltage were 6.5 nA and 30 kV, respectively. The exposed interface was then cleaned by decreasing the beam current to, e.g. 2.8 nA, 0.28 nA and 93 pA. The surface was coated with gold by ion sputtering to minimize charging during SEM. Then the exposed vertical surface was subject to SEM imaging with the electron beam inclined 38° from the film surface.

Scanning Transmission Electron Microscopy (STEM) images were acquired using a JEOL ARM-200F (with a resolution of 0.07 nm), equipped with a Cold FEG and a CEOS STEM Probe corrector. The acceleration voltage of the STEM was 200 kV. Cross sectional layer STEM sample of ca. 100 nm thickness was fabricated by FIB milling. Prior to STEM examination, as a final stage of the sample preparation, Ar^+ ion milling at 990 V was used to remove potential damage during FIB sectioning. Electron energy loss spectroscopy (EELS) and energy dispersive X-ray spectroscopy (EDX) analysis were performed with an Enfi-nium Spectrometer (Gatan, U.S.) equipped with a JEM-ARM200F. The EELS and EDX signals were simultaneously acquired by a Digital Micrograph (Gatan, U.S.) detector.

Angle resolved X-ray photoelectron spectroscopy (XPS) measurement, using a PHI Versaprobe II system, were performed to identify the depth resolved surface chemistry. The photoelectron spectra at La 4d, Sr 3d, La 3d and Co 2p emissions were used to calculate the surface cation composition. These spectra were measured at different emission angles, 0°, 45° and 70°, between the surface normal and the detector position for varying the depth resolution from bulk to the surface. For the excitation energy of 1486.6 eV, the sampling depths of photoelectrons at 0° emission angle are ~ 6 nm for Sr 3d and La 4d, and ~ 3.4 nm for La 3d and Co 2p.³² CasaXPS 2.3.16 software was used for peak analysis and quantification.

The crystallography of the as-deposited samples was confirmed by high-resolution X-ray diffraction measurements. For identifying the crystal structure, the $2\theta - \omega$ scans were measured by a high resolution four circle Bruker D8 Discover diffractometer, equipped with a Göbel mirror, 4-bounce Ge (022) channel-cut monochromator, Eulerian cradle, and a scintillation counter, using $\text{Cu K}\alpha_1$ radiation.

Scanning tunneling microscopy and spectroscopy (STM/STS) measurements were performed by a modified variable-temperature scanning tunneling microscope (VT-STM) (Omicron GmbH, Germany) with high spatial resolution from room temperature to 300 °C and in oxygen environment (10^{-3} mbar in this work). A retractable oxygen doser placed near the STM stage in the chamber was used to directly expose the sample to oxygen during the experiments. STM images were acquired in constant-current mode using Pt/Ir tips prepared by chemical etching. A tip bias voltage of 2–2.5 V and feedback tunneling current of 50–500 pA were used during measurements. For surface cleaning and *in situ* measurements, samples were heated in oxygen using a pyrolytic boron nitride (PBN) heater. To obtain high quality images and tunneling spectra, the sample was cleaned prior to the STM/STS measurements by first sputtering the surface by low energy Ar^+ (0.5 keV) for 100 seconds, followed by heating in high purity oxygen at 350 °C and 2×10^{-5} mbar pressure for 1

hour. This served to remove the water and carbon-related adsorbates from the surface due to air-exposure after film growth.

Surface morphology of LSC_{113} , LSC_{214} and $\text{LSC}_{113/214}$ VAN cathode thin films were measured by atomic force microscopy (AFM) (Veeco Metrology Nanoscope IV Scanned Probe Microscope Controller with Dimension 3100 SPM). As-prepared surface was monitored after the samples were subsequently annealed at 370 °C and 620 °C in air, in the chamber used for the electrochemical tests in this work.

Electrochemical impedance spectroscopy (EIS) measurements were performed on asymmetrical cell structures with the LSC_{113} , LSC_{214} and $\text{LSC}_{113/214}$ VAN cathode dense film structures grown on YSZ (001) single crystals ($10 \times 10 \times 0.5 \text{ mm}^3$, MTI Corporation, Richmond, CA) with $\text{Ce}_{0.9}\text{Gd}_{0.1}\text{O}_{1.95}$ (GDC) buffer layers. Gold mesh current collectors ($20 \times 20 \mu\text{m}^2$ of open area in every $40 \times 40 \mu\text{m}^2$ repeat unit in the total $7.3 \times 7.3 \text{ mm}^2$ current collector area) were deposited on the LSC thin films utilizing photolithography and RF sputtering. Porous Ag counter electrodes were applied as the counter electrode. Platinum wire leads were connected to the current collector and the counter electrode with the aid of the lab-designed mechanical clip made of Pt-Ir 20% alloy wire (4 N purity, ESPI metals, Ashland OR). EIS measurements were performed in the frequency range of 1 mHz to 1 MHz with AC amplitude of 20 mV and zero DC bias at temperatures between 320 °C and 620 °C, using the ModuLab system (Solartron Analytical) in conjunction with the FRA 1 MHz (2055A) Frequency Response Analyzer module or the Solartron 1250 impedance analyzer operated in combination with a Solartron 1286 potentiostat. ZView software (Scribner Associates, USA) was used to fit the data and construct equivalent circuits to analyze the impedance data.

3. Results

3.1 Structure and growth mechanism of the $\text{LSC}_{113/214}$ VAN films

The cross-sectional SEM image of the $\text{LSC}_{113/214}$ films on STO (001) and YSZ (001) substrates indicated a columnar structure, as shown in Fig. 2a. For the $\text{LSC}_{113/214}$ VAN films grown on the YSZ (001) substrate, the GDC buffer layer was uniform, while a columnar contrast in the VAN layer is evident. The different contrast in the films stems from the different electronic conductivities of the LSC_{113} and LSC_{214} domains. The thickness of the film, after correcting for tilting, is $\sim 160 \text{ nm}$, while the average width of the columns is $\sim 300 \text{ nm}$. The near-vertical separation of the LSC_{113} and LSC_{214} phases can also be observed in the high resolution STEM image of the atomic structure in Fig. 2b. Further detailed STEM-EDX analysis shows no increase or decrease of Sr content across the interface region (Fig. 2c). The $\text{Sr}/(\text{Sr} + \text{La})$ ratios are 0.32 in LSC_{113} and 0.45 in LSC_{214} columns (Table S2[†]), results consistent with the AES analysis (Table S1[†]).

Phase identification was also achieved by mapping the Co LMM Auger signal intensity. Fig. 3a shows the concentration distribution of Co cations on the sample surface mapped spatially by the Auger nano-probe. The intensity of the Co peak in the Auger spectrum is

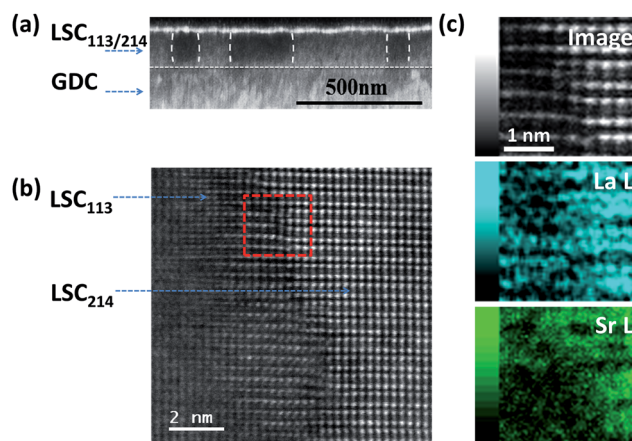


Fig. 2 (a) Cross-sectional SEM image of the $\text{LSC}_{113/214}$ VAN film on the YSZ (001) substrate with a GDC interlayer. (b) STEM image near the interface of LSC_{113} and LSC_{214} columns. (c) Zoomed-in STEM image of the region marked by the red dashed square in (b) and STEM-EDX mapping of La L and Sr L signals in that region.

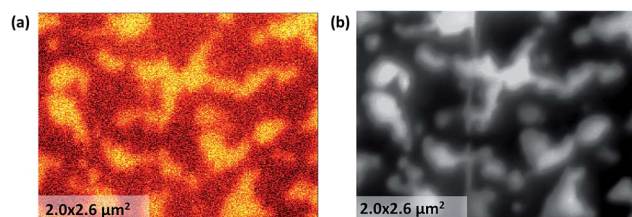


Fig. 3 (a) Auger spectrum mapping of Co cation concentration at the surface of the $\text{LSC}_{113/214}$ film on STO (100) substrate, showing two different domains coexisting in the film. (b) The SEM image of the same area as in (a).

an indication of the Co concentration in the sample. The number density (atomic concentration) of Co is $1.8 \times 10^{28} \text{ m}^{-3}$ and $5.6 \times 10^{27} \text{ m}^{-3}$ for stoichiometric LSC_{113} and LSC_{214} , respectively. The bright regions are the Co rich phase assigned to the LSC_{113} domains, while the dark regions are assigned to the LSC_{214} domains. The image contrast, as recorded by SEM (Fig. 3b), matches the Co distribution shown in Fig. 3a. The contrast on the SEM image originates from the differences in the conductivity of these two phases (LSC_{214} is more insulating than LSC_{113} (ref. 33 and 34)). Image contrast and the grain (or domain) size on the order of hundreds of nm are also consistent with the cross-sectional SEM image in Fig. 2.

The surface morphology of the VAN structure on STO (001) and YSZ/GDC (001) acquired by STM are shown in Fig. 4, along with the corresponding height profile. The measured grain size, between 300 to 500 nm, is consistent with those observed by SEM. The surface of the $\text{LSC}_{113/214}$ VAN film shows interesting features including two types of domains, spiral and layered, pointing to two different growth mechanisms. Later we show that the spiral growth zones consist of LSC_{113} and the layered growth zones consist of LSC_{214} . Such spiral growth of perovskite type oxides was also found and studied in other material systems.^{35–37} Each of these spiral grains incorporates a screw dislocation. The screw

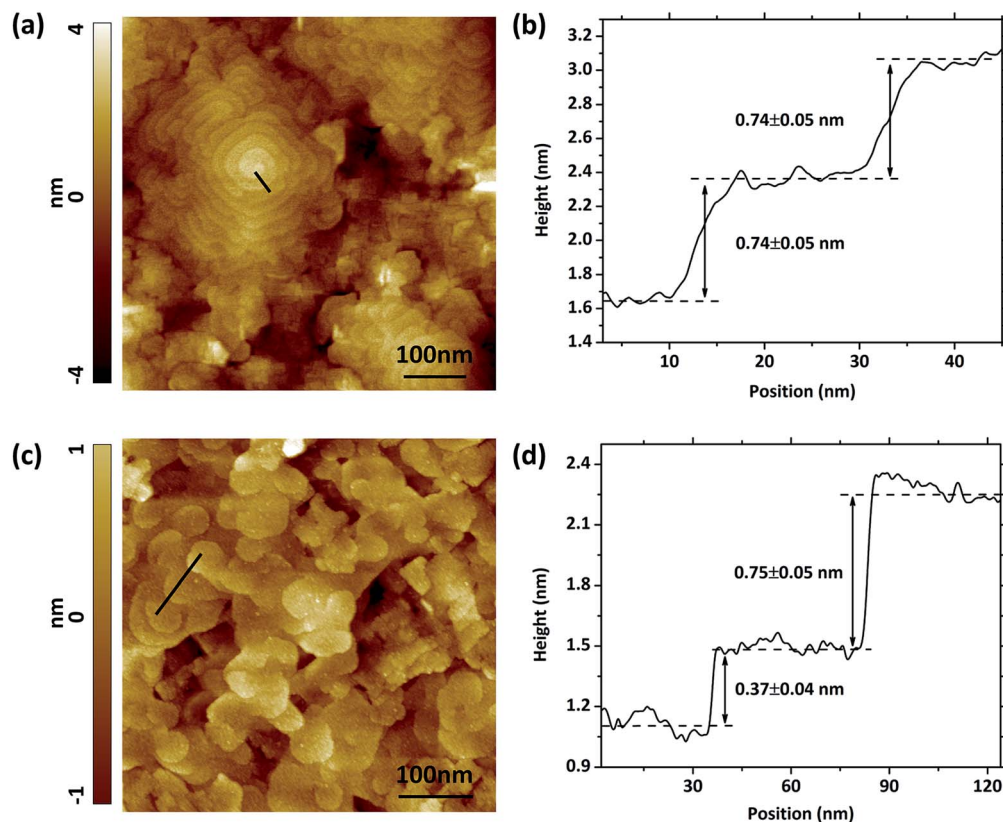


Fig. 4 STM image of $\text{LSC}_{113/214}$ VAN structure surface on (a) STO (001) and (c) GDC/YSZ (001) at room temperature. Imaging condition: $V_{\text{bias}} = 2.5$ V, $I_{\text{tunnel}} = 500$ pA. (b) and (d) height profiles of the black lines in the STM images in (a) and (c), respectively.

dislocations serve as growth centers for the crystal, the step associated with the dislocation winds itself in such a spiral manner that the dislocation continuously generates steps. The crystal is grown by adding atoms onto the spirally extended steps, resulting in a columnar grain structure.³⁷ Such a growth mode driven by screw dislocations was believed to be the reason for spontaneous nanotube growth in various materials, such as $\text{Co}(\text{OH})_2$ and ZnO .^{38–40} This mechanism could also explain the growth mechanism of the nano-column structure in the $\text{LSC}_{113/214}$ VAN films. The screw dislocations were observed on the VAN films grown both on STO (Fig. 4a) and on YSZ/GDC (Fig. 4c) substrates. According to the STM images of the surfaces of VAN films grown on STO and YSZ/GDC, most terraces around the dislocations at the surface are atomically flat and separated by growth steps, one or two LSC_{113} unit cells high (Fig. 4b and d). In contrast, no such feature was observed on the single phase LSC_{113} and LSC_{214} films deposited under the same conditions and on the same substrates. This result suggests that the spiral pattern is also assisted by the coherence and stress from the $\text{LSC}_{113/214}$ vertical interfaces. In the next section, we provide a detailed strain analysis of these composite films.

3.2 Strain state of $\text{LSC}_{113/214}$ VAN films

The $2\theta - \omega$ scans for the VAN films on STO (001) and YSZ (001) with GDC buffer layer are shown in Fig. 5. X-ray diffraction analysis revealed the films to be oriented with their c -axes

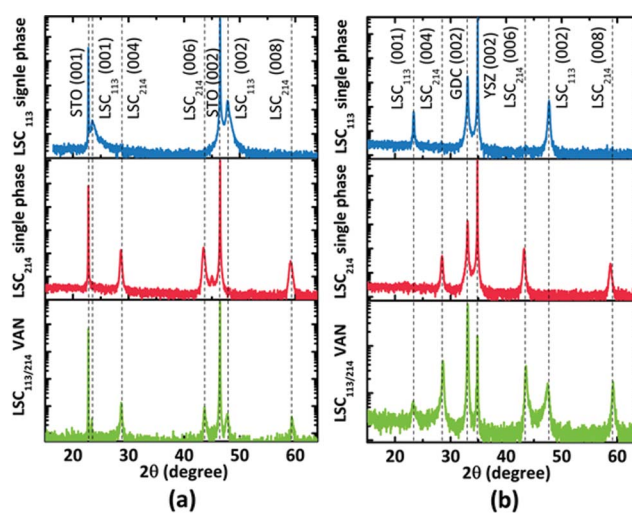


Fig. 5 The $2\theta - \omega$ scans with logarithmic intensity scale of (a) LSC_{113} , LSC_{214} , and $\text{LSC}_{113/214}$ VAN on STO (001) and (b) LSC_{113} , LSC_{214} , and $\text{LSC}_{113/214}$ VAN on GDC/YSZ (001). The diffraction patterns show only the 00 l diffraction peaks of LSC.

perpendicular to the substrate. Only the 00 l reflections of LSC_{113} and LSC_{214} are present in the diffraction pattern; no peaks from any other impurity phase or orientation were observed. However, when we compare this diffraction pattern

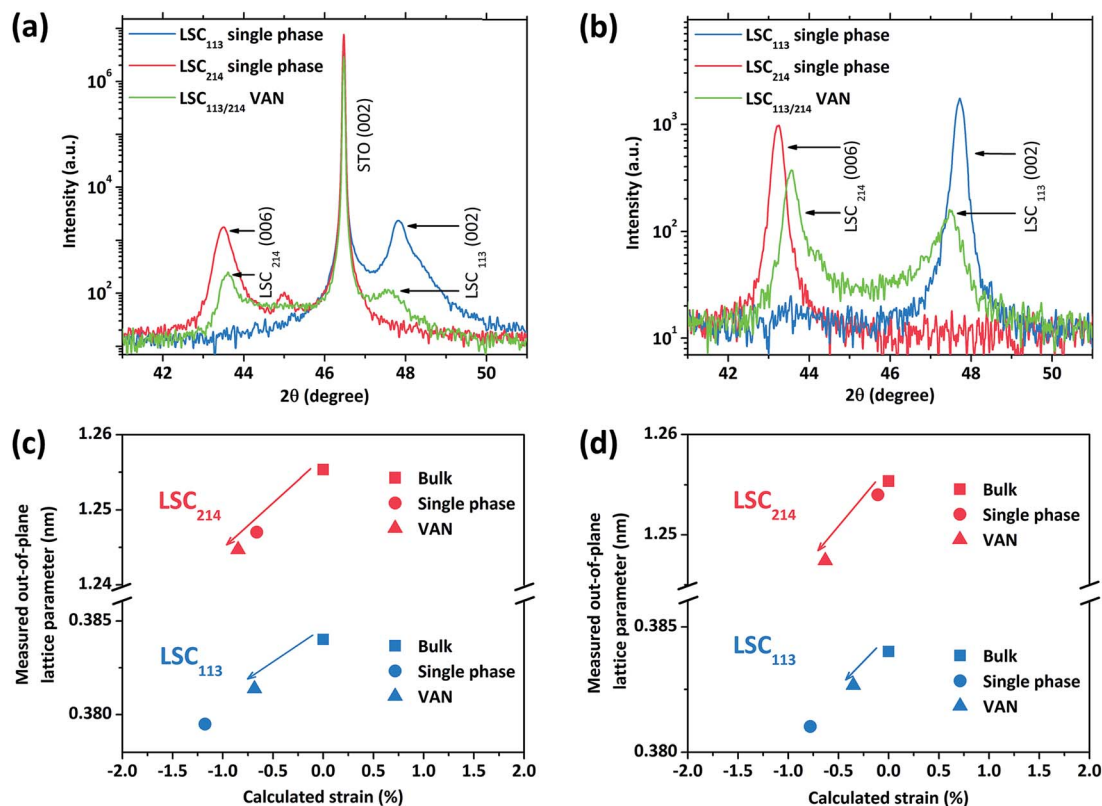


Fig. 6 X-ray diffraction data for the LSC_{113/214} VAN structure compared with single phase reference films of LSC₁₁₃ and LSC₂₁₄. $2\theta - \omega$ scans near the LSC₁₁₃ (002) and LSC₂₁₄ (006) of LSC₁₁₃, LSC₂₁₄, and LSC_{113/214} VAN on (a) STO (001) and (b) GDC/YSZ (001). The out-of-plane lattice constants versus calculated out-of-plane strain (with respect to bulk value) in LSC₁₁₃, LSC₂₁₄, and LSC_{113/214} VAN on (c) STO (001) and (d) GDC/YSZ (001).

with single phase reference films, both the LSC₁₁₃ and LSC₂₁₄ peaks in the VAN have shifted with respect to their corresponding single phase patterns, indicating that the vertical strain state in each phase is altered in the LSC_{113/214} VAN structure.

Fig. 6a and b show the regions near the LSC₁₁₃ (002) and LSC₂₁₄ (006) peaks for the VAN films compared with the single phase films. For the single phase LSC₁₁₃ and LSC₂₁₄ films grown on GDC/YSZ (001), the out-of-plane lattice parameters are 3.810 Å and 12.540 Å, which are lower than the bulk values of 3.840 Å and 12.553 Å (found from X-ray powder diffraction measurement of the LSC₁₁₃ and LSC₂₁₄ targets used for PLD). The strain states of LSC films on STO and GDC/YSZ substrates are consistent with those reported in the literature.^{16,26,41} The strain state of the LSC/STO system can be explained by the lattice mismatch between film and substrate. But the origin of strain on LSC/GDC/YSZ is not well understood, since it cannot be explained by the confinement of the LSC film in plane by the GDC/YSZ (001) substrate, which would result in an opposite strain state at room temperature. It might be a consequence of different thermal expansion coefficients between the YSZ and LSC films as la O' *et al.* pointed out in their report.⁴¹ The physical origin of the strain state of the LSC films on YSZ substrate is out of the scope of this paper.

In the VAN structure, the out-of-plane lattice parameter is a direct indication of the strain state.⁴² Fig. 6c and d show the out-of-plane lattice parameters of each phase (LSC₁₁₃ and LSC₂₁₄) in the VAN films versus the out-of-plane strain. Out-of-plane strain is calculated from the difference between the measured out-of-plane lattice parameter values for thin films and the known lattice parameter values for bulk. The results of the strain state on STO and YSZ substrates are very similar. The out-of-plane lattice parameter of LSC₁₁₃ in the VAN structure is larger than that of the single phase LSC₁₁₃, while the LSC₂₁₄ phase has a smaller out-of-plane lattice parameter in the VAN structure than in the single phase reference film. This result shows that the vertical strain states of LSC₁₁₃ and LSC₂₁₄ have been changed in the VAN structure, with extra tensile (compressive) strain imposed to LSC₁₁₃ (LSC₂₁₄) within the respective domains. However, the interface strain state seems to be still mainly controlled by the lateral lattice mismatch between the film and the substrate. The transition from lateral strain control to vertical strain control depends on the geometry of the columnar grains. When the vertical interface area for a columnar grain exceeds the film/substrate interface area, the vertical strain would play a dominant role. Since this study is focusing on the correlation between electronic structure, surface chemistry and ORR kinetics, we aim to compare the results with the single phase reference films, which only have lateral strain and no

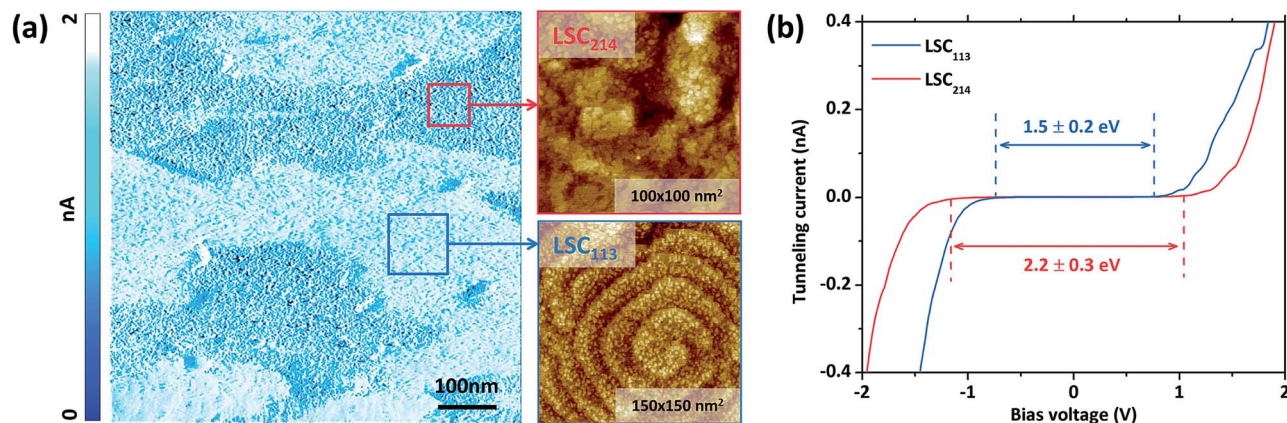


Fig. 7 Electronic and topographic features of the surface of LSC_{113/214} VAN thin films on STO (001) (VAN/STO). (a) Tunneling feedback current map (negative image), with zoomed in topography. The contrast of the tunneling feedback current image indicates different conductivity and therefore different phase. (b) Tunneling current versus bias data on LSC₁₁₃ and LSC₂₁₄ domains. LSC₁₁₃ domains in the VAN have a similar surface energy gap (1.5 ± 0.2 eV) as on the single phase LSC₁₁₃ reference films, while LSC₂₁₄ domains in the VAN have a measurable energy gap of 2.2 ± 0.3 eV.

vertical strain. Therefore, we retain the lateral strain state of the VAN films to be substrate controlled (just as in the single phase reference films) by keeping the film thickness (of 160 nm) less than the width of each column (300–500 nm).

3.3 Surface electronic structure of VAN films at room temperature

The phase assignment within the LSC_{113/214} composite is also confirmed by the tunneling current mapping and tunneling spectroscopy measurements (Fig. 7). Fig. 7a shows the tunneling current image with the zoomed-in topography image on the right. The contrast in the tunneling current image indicates the different conductivities of the respective regions: the regions with higher conductivity show the spiral growth pattern, while the darker regions have the layered structure. The tunneling spectroscopy (Fig. 7b) also shows the spiral grains to have an energy gap of about 1.5 ± 0.2 eV, while the layered region to have an energy gap of about 2.2 ± 0.3 eV and 2.1 ± 0.2 eV on STO and YSZ, respectively. Because LSC₁₁₃ is more conducting and has a smaller energy gap than LSC₂₁₄,¹⁸ we assign the spiral regions to be consisting of LSC₁₁₃ and the layered regions to be consisting of LSC₂₁₄. Our previous work has shown the LSC₁₁₃ single phase surface energy gap to be 1.5 eV \pm 0.2 eV,²⁶ which is consistent with the LSC₁₁₃ domains in the VAN structure here.

It should be noted that the STM measurements under room temperature conditions could not be successfully performed on the single phase LSC₂₁₄ given its insulating nature. On the other hand, it was possible to perform STM and STS measurements on the LSC₂₁₄ phase in the VAN film, and the energy gap at the surface is 2.2 ± 0.3 eV and 2.1 ± 0.2 eV on STO and YSZ, respectively. In addition, the energy gap is quite uniform over the LSC₂₁₄ domains. STM of the LSC₂₁₄ domains within the VAN film is assisted by the presence of LSC₁₁₃ domains that increase the overall electronic conductivity of the composite film.

3.4 Surface electronic structure of VAN films at elevated temperature

Further investigation of the electronic structure of the film was carried out as a function of temperature. The energy gaps of LSC₁₁₃ and LSC₂₁₄ surfaces in the VAN structure were successively measured at room temperature, 100 °C, 200 °C, 250 °C, 300 °C and finally at room temperature again upon subsequent cooling from 300 °C, in 10^{-3} mbar of pure oxygen. The same measurements were also taken on the single phase reference films (Fig. 8a and b). The energy gap of LSC₁₁₃ in the VAN and in the single phase film have a very similar behavior, going from 1.5 ± 0.2 eV at room temperature to metallic-like behavior with no energy gap at and above 250 °C. After cooling back down to room temperature, the energy gap recovers to 1.5 ± 0.2 eV, showing the reversibility of the semiconductor-metallic transition at the surface. The semiconductor-metallic transition arises from the creation of oxygen vacancy energy levels in the gap, as we reported in our previous work on LSC₁₁₃ single phase thin films.²⁶

On the other hand, the temperature dependence of the energy gap at the surface of the LSC₂₁₄ domains in the VAN structure is very different from that of the LSC₂₁₄ single phase films. At and above 250 °C, the surface energy gap of LSC₂₁₄ deviates from that on single phase LSC₂₁₄ by about 1 eV. Comparing Fig. 8a and b, the electronic structure at the LSC₂₁₄ surface in the VAN structure follows the LSC₁₁₃ phase by becoming metallic-like above 250 °C. These results are consistent with the “electronic activation behavior” reported in our recent work for the LSC₁₁₃/LSC₂₁₄ multilayer structures (Fig. 8, ML data points¹⁸). At elevated temperatures, the LSC₁₁₃ surface is easily reduced, forming oxygen vacancies.²⁶ This serves to raise the electron chemical potential (Fermi level) and decrease the chemical potential of oxygen in the LSC₁₁₃ phase.⁴³ This would be expected to drive oxygen from LSC₂₁₄ into LSC₁₁₃ (ref. 44) and electrons from LSC₁₁₃ to LSC₂₁₄.¹⁸ The injection of

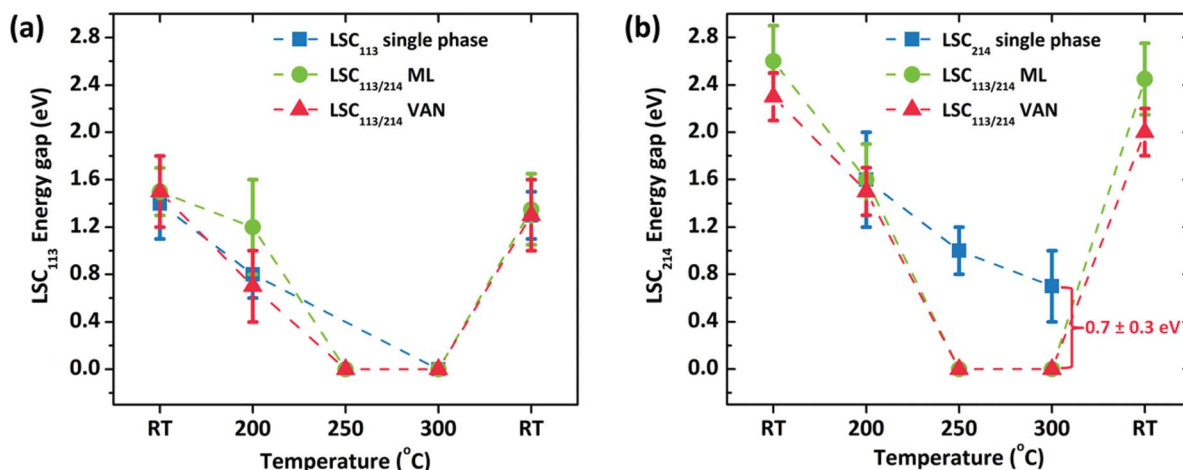


Fig. 8 Temperature dependence of the energy gap of (a) LSC_{113} and (b) LSC_{214} in single phase, multilayer and VAN/STO structure. Note that the surface energy gap variations with temperature in ML and VAN are quite similar for both LSC_{113} and LSC_{214} phases. The data on the multilayer system comes from ref. 18 and the data on the LSC_{113} comes from ref. 26.

electrons from LSC_{113} to LSC_{214} and the creation of defect states in LSC_{214} raises the Fermi level into the conduction band in the LSC_{214} phase, resulting in the disappearance of the energy gap as shown in Fig. 8b. Exchange of oxygen defects and electronic defects across the interfaces also enables charge neutrality over the width of the grain surfaces in the VAN.

3.5 Surface electrochemical activity of VAN films and electronic activation mechanism

All the electrochemical impedance spectra measured for LSC_{113} , LSC_{214} and $\text{LSC}_{113/214}$ VAN thin film electrodes consist of one dominating semicircle at low frequencies, an additional arc at intermediate frequencies and a non-zero intercept at the x -axis at higher frequencies. Fig. 9(a) shows a typical impedance spectrum obtained for the $\text{LSC}_{113/214}$ VAN thin film electrode on GDC/YSZ in air. As shown in the inset, the spectrum can be modeled by a resistor in series with two R/Q circuits (R/Q: a resistor in parallel with a constant phase element, CPE). CPEs are used to take into account the possible heterogeneities in the electrodes resulting in “depressed” arcs not well represented by ideal capacitors.² The offset resistance (R_1) shows no pO_2 or DC bias dependence and is characterized by an activation energy of 1.07 ± 0.07 eV, reflecting the YSZ ohmic contribution in series to the overall cell impedance. The additional arc between the offset resistance and the large semicircle at low frequencies also shows no pO_2 dependence and is attributed to the ionic transfer resistance at the electrode/electrolyte interface. The real component of the low frequency impedance (R_3) was found to increase with decreasing pO_2 , a feature typical of the oxygen exchange resistance.⁴⁵ This assignment is further supported by the exceptionally large equivalent capacitance⁴⁶ ($2\text{--}5$ mF cm^{-2}), derived from CPE_3 indicative of a chemical capacitance, as reported for other thin film MIEC systems.^{7,47} From the fitting procedure, the n -values of the CPE_3 show no significant difference between the single-phase and VAN films, giving 0.84 ± 0.01

for LSC_{113} , 0.81 ± 0.02 for LSC_{214} and 0.78 ± 0.04 for $\text{LSC}_{113/214}$ VAN film cathodes, respectively.

Fig. 9(b) shows the temperature dependence of the resistance of the surface to oxygen exchange, in terms of an area specific resistance (ASR) in air, derived from element R_3 , for the LSC_{113} and LSC_{214} single phase thin film electrodes and for the $\text{LSC}_{113/214}$ VAN film electrode for the temperature range of 320–397 °C. The ORR activity of VAN film electrodes, which is inversely related to this surface exchange ASR, is clearly seen to be enhanced by about one order of magnitude, compared to that of the LSC_{113} and LSC_{214} single phase electrodes. The range of the derived activation energies, 1.35–1.68 eV, are similar to those previously reported for LSC electrodes.^{13,27,48–52} However, the enhanced ORR activity disappears at higher temperatures, in the range of 445 °C to 620 °C in this work. Fig. 10 shows the temperature dependence of the ASR of the LSC_{113} single phase and $\text{LSC}_{113/214}$ VAN film electrodes measured in air and at temperatures of 445 °C–546 °C. The ASR is observed to systematically increase at the initial temperature of 445 °C during subsequent measurements taken 30 minutes apart. After the ASR reached a stable value, the measurement temperature was increased up to 546 °C and then decreased back to 445 °C. The surface exchange ASR of the LSC_{113} single phase and of the $\text{LSC}_{113/214}$ VAN films reached similar values during this process, a signature of the degradation of the surface activity of both the LSC_{113} and $\text{LSC}_{113/214}$ VAN electrodes. The next section will present the evolution of the surface cation composition and microstructure to explain this degradation process.

3.6 Evolution of surface microstructure and cation chemistry upon thermal annealing

The electrochemical impedance results indicate a significant degradation of the surfaces at elevated temperatures, above 400 °C (specifically shown at 450–620 °C in this work). This degradation of the surface reactivity suggests some form of

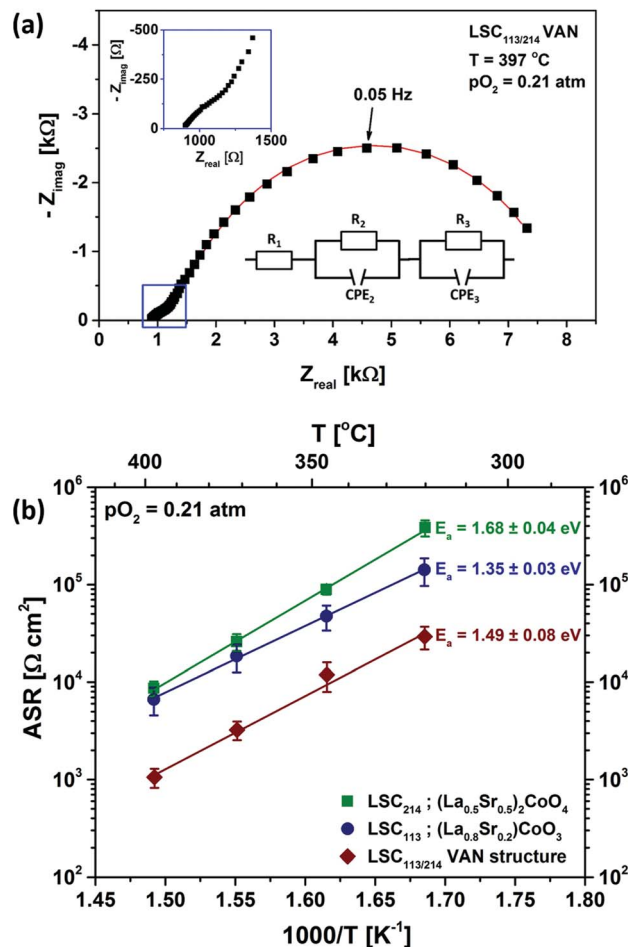


Fig. 9 (a) A typical electrochemical impedance spectrum measured for an LSC_{113/214} VAN thin film electrode on GDC/YSZ (001) at 397 °C and in air. All the impedance spectra of LSC₁₁₃ and LSC₂₁₄ thin film electrodes show similar characteristics (Fig. S2†). The square dots are experimental data, while the solid line represents the best fit obtained with the equivalent circuit shown in the bottom inset. Variables of the circuit model are explained in the text. The top inset shows a magnification of the high frequency regime. (b) Temperature dependence of the area specific resistance (ASR) of oxygen surface exchange reaction at the surface of LSC₁₁₃ and LSC₂₁₄ single phase film electrodes and of LSC_{113/214} VAN film electrode measured in air and at 320 °C–397 °C.

chemical aging at the surface as reported for LSC by Kubicek *et al.*⁵³ and by us⁵⁴ earlier. To identify the source of the degradation on LSC_{113/214} VAN films at elevated temperatures, an equivalent set of as-prepared LSC_{113/214} VAN and single phase LSC₁₁₃ and LSC₂₁₄ reference samples were annealed for 10 hours at 370 °C and at 620 °C in air, using the same setup and conditions as in the EIS measurements. These were subsequently subjected to AFM and XPS analysis to examine how the surface microstructure and chemistry evolves at elevated temperatures.

As shown Fig. 11a, the as-prepared LSC₁₁₃ single phase film was characterized by a smooth surface with grains of a few hundreds of nm wide. While no change in surface morphology was detected in AFM following annealing at 370 °C (Fig. 11b), smaller particles appeared across the entire surface (some

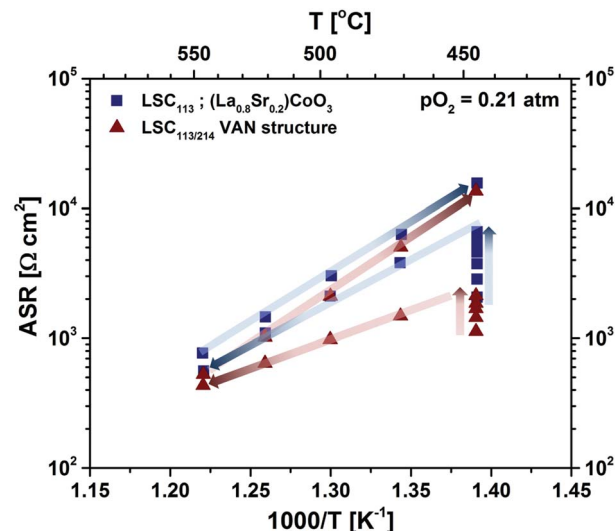


Fig. 10 Temperature dependence of the area specific resistance (ASR) of LSC₁₁₃ single phase film electrode (blue squares) and of LSC_{113/214} VAN film electrode (red triangles) measured in air and at 445 °C–546 °C. The blue and red arrows indicate the measurement sequence on the LSC₁₁₃ single phase and the LSC_{113/214} VAN film electrodes, respectively. The ASR was monitored while the samples were kept at 445 °C during measurements taken 30 minutes apart. After the ASR reached a stable value at 445 °C, the measurement temperature was increased up to 546 °C and then decreased back to 445 °C.

preferentially at grain boundaries) after annealing at 620 °C (Fig. 11c). As-prepared LSC₂₁₄ single phase film, on the other hand, showed a rougher grain structure (Fig. 11d). After thermal annealing at 620 °C in air, the surface became relatively less rough but many particles evidently remain (Fig. 11f) at the surface. Within the resolution limit of the AFM image, the surface morphology and roughness of the VAN film annealed at 370 °C does not change from the as-prepared state (Fig. 11g and h). However, the surface roughness increases, along with the formation of large particles at the surface and the disappearance of the spiral domain, after annealing at 620 °C. Interestingly, the areas where the particles are formed can be clearly separated by the area without the particles (as seen in Fig. 12b), indicating that part of the film surface is not segregating. By comparing the size and shape of the film features (*i.e.* disappearance of the spiral patterns, and the remaining flat faceted/cornered features in Fig. 12b), the area with and without particles can be assigned to LSC₁₁₃ and LSC₂₁₄ domains, respectively, on the VAN film. This indicates that the presence of LSC₁₁₃ domains enables a more stable LSC₂₁₄ surface that does not form precipitated particles neither at the as-prepared state and nor at the annealed state.

The surface roughening in the VAN film is accompanied by a sharp enrichment of the A-site cations (La and Sr), *i.e.* a larger (Sr + La)/Co ratio (Fig. 13g and i) at/near the surface. Furthermore, as shown from the increase of the (Sr + La)/Co quantity from 0° (deeper into the bulk by 6 nm) to 70° (within 2 nm of the surface), the enrichment of the A-site cations at 620 °C is originating at/near the surface of the VAN films, concurrent with the

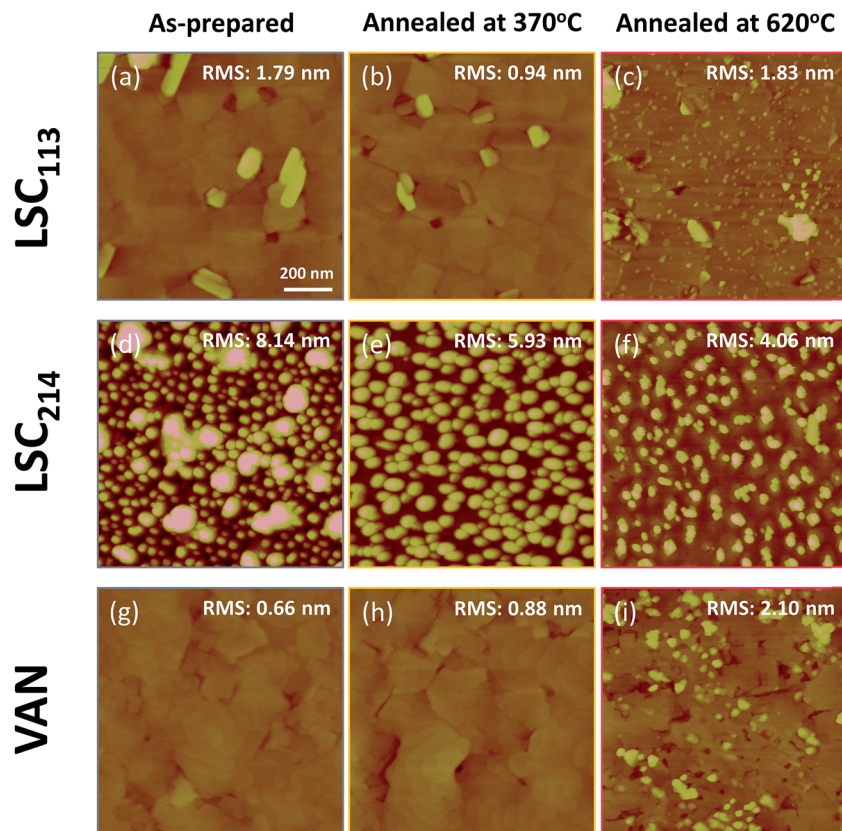


Fig. 11 Atomic force microscopy images ($1\ \mu\text{m} \times 1\ \mu\text{m}$) of the $\text{LSC}_{113/214}$ VAN, LSC_{113} and LSC_{214} films on GDC/YSZ (001) substrate at different conditions: as-prepared, annealed for 10 hours at 370°C and at 620°C in air. The common height-scale for each image is 0–30 nm.

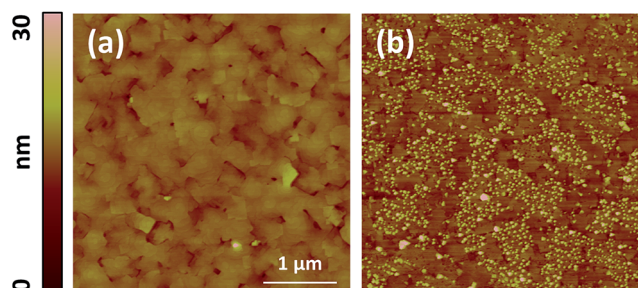


Fig. 12 Atomic force microscopy images ($5\ \mu\text{m} \times 5\ \mu\text{m}$) of the $\text{LSC}_{113/214}$ VAN films on GDC/YSZ (001) substrate at different conditions: (a) as-prepared and (b) annealed for 10 hours at 620°C in air.

formation of the particles shown in Fig. 11 and 12. Similarly to our and others' previous findings,^{29,54,55} such A-site enrichment exists in the formation of insulating phases,^{54,56,57} as also seen in this work from the AFM images (Fig. 11 and 12) and from the analysis of the Sr 3d spectrum (Fig. S1†). Such chemical, electronic and phase changes at the surface contribute to surface reactivity degradation of the perovskite and perovskite-related phases, and thus, slows the ORR kinetics at the surface of the $\text{LSC}_{113/214}$ VAN films as found in our EIS experiments.

Very interestingly, comparison of the cation composition on the $\text{LSC}_{113/214}$ VAN film with that on the single phase LSC_{113} and

LSC_{214} reference films reveals that the VAN surface is chemically more stable than the surfaces of LSC_{214} and LSC_{113} alone. The magnitude of the total A-site cation enrichment, denoted by the $(\text{Sr} + \text{La})/\text{Co}$ ratio, at the VAN film surface at 620°C is (~ 4) much smaller than that of the LSC_{214} (~ 12) and closer to that of the LSC_{113} surface (~ 3) (Fig. 13c, f and i). Sr enrichment at the A-site, denoted by the $\text{Sr}/(\text{Sr} + \text{La})$ ratio, at the VAN surface is close to the bulk nominal value both at 370°C and 620°C , while that on LSC_{113} is greater than the bulk nominal level. This result indicates that the LSC_{113} phase in the VAN structure may also play a role in stabilizing the $(\text{La} + \text{Sr})/\text{Co}$ ratio and avoid (or minimize) phase separation of Sr- and La-rich oxides at the LSC_{214} domain surface. At the same time, the total Sr enrichment at the surface is suppressed on the VAN surface. These signatures of chemical stabilization can also contribute to a superior electrochemical performance of the $\text{LSC}_{113/214}$ VAN films.

4. Discussion

This work had two motivations: (1) to examine the validity of the electronic activation mechanism in a columnar composite made of $\text{LSC}_{113/214}$ that provides a more controlled structure for embedding hetero-interfaces in cathodes, and (2) to uncover whether there are any additional mechanisms that contribute to the enhancement of the ORR reactivity of the $\text{LSC}_{113/214}$ hetero-

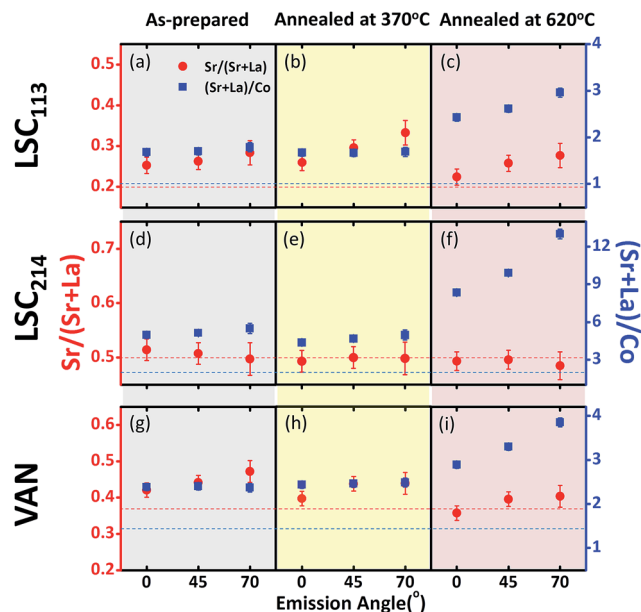


Fig. 13 Sr/(Sr + La) and (Sr + La)/Co ratios deduced from X-ray photoelectron spectroscopy measurement and analysis of the La 4d, Sr 3d, La 3d and Co 2p emissions, on the VAN, LSC₁₁₃ and LSC₂₁₄ films that are in the as-prepared state and that were annealed at 370 °C and at 620 °C in air for 10 hours. The photo-electron emission angles of 0°, 45° and 70° indicate the depth sensitivity, going from deeper to more surface sensitive signals, respectively. The determination of bulk nominal Sr/(Sr + La) and (Sr + La)/Co values for VAN are based on the 3 : 2 molar ratio of LSC₁₁₃ and LSC₂₁₄ in LSC_{113/214} composite target (see Section 2. Experimental methods).

system in a structure that is feasible for electrochemical measurements. The vertically aligned nanocomposite made of LSC_{113/214} provided the means to probe both of these purposes in this work.

From the tunneling spectroscopy measurements (Fig. 7), we confirmed that the LSC₂₁₄ phase in the VAN structure is electronically activated, in a similar way as was shown within the LSC_{113/214} multilayers in our recent work.¹⁸ The effective activation area extends to the entire LSC₂₁₄ domains whose dimensions ranges from 50 to 300 nm. Such large spatial extent of electronic activation could be explained by electron injection¹⁸ accompanied by exchange of charged oxygen defects (oxygen vacancies and interstitials)^{28,44} at LSC_{113/214} interfaces that enables long-range charge neutrality in the system.

The apparent electronic activation of the LSC₂₁₄ domains in the VAN structure is expected to have the following impact on the ORR kinetics. The upshift of the Fermi level that leads to the disappearance of the energy gap on LSC₂₁₄ in VAN at elevated temperatures (250–300 °C) represents a larger concentration of free electrons on this originally p-type material, leading to faster oxygen reduction kinetics on LSC₂₁₄ domains. In this study, we observed 10 times enhancement of ORR kinetics instead of 3 orders of magnitude as reported in the literature.^{14,15} One of the reasons for the lesser enhancement could be the strongly anisotropic structure and oxygen incorporation properties of LSC₂₁₄. Given that the LSC₂₁₄ [100] direction, which is the fast

oxygen incorporation and transport path, is parallel to the sample surface, the VAN structure on YSZ (001) substrate could not benefit from the 10² times ORR enhancement predicted by Han and Yildiz due to the anisotropic oxygen incorporation kinetics through LSC₂₁₄ (100) channel.²⁰

The combined XPS, AFM and EIS measurements on the LSC₁₁₃, LSC₂₁₄ and LSC_{113/214} VAN film electrodes revealed the superior stability of the cation composition on the LSC_{113/214} VAN surface could be another source of the higher ORR activity. The reduced enrichment of Sr and La cations at the surface of the VAN films allows for more pristine perovskite and Ruddlesden Popper terminations, and minimizes or partially avoids the coverage of the surface by insulating phases such as Sr- and La-rich oxides or hydroxides that block the ORR kinetics. The LSC_{113/214} VAN structure films are stable at lower temperatures (320–400 °C). At higher temperatures, on the other hand, all the films, including the LSC_{113/214} VAN film, suffered from a strong time-dependent degradation. Although the surface chemistry of the VAN is more stable than the single phase films, it is sufficiently segregated that the degradation of the ORR kinetics is still quite evident. Based on the electronic activation and the decrease of the detrimental surface segregation found at the VAN surface in this work, future work that identifies more stable hetero-structures while retaining the electronic coupling is warranted.

We have shown that the VAN arrangement of the LSC perovskite and Ruddlesden-Popper phases resulted in the generation of line defects (screw dislocations) perpendicular to the surface of the VAN structure in the LSC₁₁₃ domains (Fig. 4 and 7). The density of screw dislocations is about $N = 60 \mu\text{m}^{-2}$ as counted from the STM images. We note that the effect of such line defects on the surface ORR kinetics is still not clear. If we assume that the ORR kinetics enhancement is only due to the screw dislocations, then we could get an estimation of the relative enhancement at the dislocations based on the following equation: $\phi k_{\text{chem}}^{\text{disl}} + (1 - \phi)k_{\text{chem}}^{\text{LSC}} = k_{\text{chem}}^{\text{VAN}} = 10 \times k_{\text{chem}}^{\text{LSC}}$, where ϕ is the percentage of dislocation activated area, k_{chem} is the chemical surface exchange coefficient. Assuming the activation radius of each dislocation is $r = 1\text{--}3 \text{ nm}$, then $\phi = N \times \pi \times r^2$ is about $10^{-4} - 10^{-3}$, which gives $k_{\text{chem}}^{\text{disl}} \approx 10^4 \text{ to } 10^5 \times k_{\text{chem}}^{\text{LSC}}$. Thus, the ORR kinetics would be expected to have at least four or five order of magnitude enhancement at dislocations in order to obtain one order of magnitude overall enhancement. There is no evidence showing such surface ORR enhancement by screw dislocations in the literature. Therefore, we could not attribute the 10 times ORR kinetics improvement entirely to the effect of screw dislocations.

The VAN structure has shown potential as a high performance intermediate temperature SOFC cathode. Some aspects still need to be improved to further enhance the overall ORR kinetics. First of all, as mentioned in the discussion of the electronic activation mechanism, the fast oxygen incorporation path, LSC₂₁₄ (100), is lying parallel to the surface instead of normal to the surface. By synthesizing LSC₂₁₄ (100) vertical to the surface in the VAN structure and by finding ways to avoid detrimental cation segregation at the surface, we could expect further enhancement of ORR kinetics, besides the electronic

activation enhancement. Chemically optimizing the doping levels of both the A- and B-site cations or exploring other coupled perovskite/Ruddlesden-Popper material systems, to get better electronic and ionic conductivity and stability, also provides unlimited opportunities to further improve the ORR kinetics. The control of microstructure could be achieved by varying deposition parameters, substrate interface and ratio of phase composition. Additional treatment of VAN structure, either by thermal annealing in varying oxygen pressures or by selective etching, could also be an effective way to tailor desirable microstructural and chemical properties for higher ORR activity.

5. Conclusion

Vertically aligned nanocomposites $\text{LSC}_{113/214}$ were synthesized and examined with respect to their electronic structure, surface chemistry and electrochemical performance. A number of interesting features that relate to the performance of these VAN films were found. Vertically aligned nano-scale columns of LSC_{113} and LSC_{214} were formed coherently on the STO (001) and YSZ/GDC (001) substrates. The surface electronic structure of LSC_{214} in VAN was modified compared to single phase LSC_{214} films. Upon the onset of reduction in LSC_{113} at 250 °C and above, the exposed LSC_{214} grain surfaces were found to be electronically activated, with a complete disappearance of the energy gap in contrast to the $\sim 0.7\text{--}1$ eV energy gap at the surface of the single phase LSC_{214} films, as detected by *in situ* STM and STS. Electrochemical impedance analysis showed a 10-fold increase of surface oxygen exchange kinetics on the $\text{LSC}_{113/214}$ VAN cathodes compared to the LSC_{113} and LSC_{214} single phase film cathodes at 320–400 °C, demonstrating improved performance enabled by the hetero-interfaces in a controlled microstructure. Combined XPS, AFM and EIS measurements also revealed superior stability of the cation composition on the $\text{LSC}_{113/214}$ VAN film compared to the detrimental segregation and phase separation of Sr- and La-rich phases at the surfaces of the LSC_{113} and LSC_{214} single phase films. Both the electronic activation and the relatively more stable cation composition at the $\text{LSC}_{113/214}$ VAN films are likely to be mechanisms that render these hetero-systems more highly reactive to oxygen reduction reaction. However, above 400 °C, the stability of the surface chemistry of the $\text{LSC}_{113/214}$ heterosystem appears to become an issue, leading to the degradation of the oxygen reduction kinetics.

In concluding, we identify the VAN composite structure as a highly promising approach for achieving enhanced cathode performance and stability. While the $\text{LSC}_{113/214}$ composite shows reduced detrimental segregation and phase separation of Sr- and La-rich phases at its surfaces, nevertheless, the degradation of the surface remains significant at temperatures above 400 °C. This stability issue arises because of intrinsic properties of the $\text{LSC}_{113/214}$ composition itself, and is not because of the VAN structure. This finding is particularly significant since the instability of the $\text{LSC}_{113/214}$ hetero-structure was not previously discussed in the works of Sase *et al.*^{14,15} and Crumlin *et al.*^{16,58} that focused only on the initial performance of this composite.

While this is a partially negative finding, it aids in directing future research towards the identification of alternatives that are inherently more stable, while retaining their high reactivity to ORR. Furthermore, within our knowledge, this is the first study to adopt a vertically aligned nano-structure composite designed to enhance the electrochemical activity by virtue of the formation of internal hetero-interfaces. These interfaces offer means for further enhancing the ORR activity of the LSC_{214} phase by enhancing its charge transfer capability and minimizing La and Sr segregation to its surface. Such VAN composite structures enable finer tuning of reactivity and stability by control of orientation, strain and phase fraction of each of the phases within the composite film. Work is ongoing by the authors to identify more highly stable hetero-structure VAN compositions with high ORR reactivity.

Acknowledgements

This work was supported by the US-DOE Basic Energy Sciences, Grant no. DE-SC0002633 at MIT. The cross sectional SEM, X-ray diffraction, X-ray photoelectron spectroscopy and Auger electron spectroscopy measurements were performed at the Center of Materials Science and Engineering, an NSF MRSEC facility at MIT. T. D. and K. S. acknowledge financial support from the Progress-100 program at Kyushu University. JJK thanks the Kwanjeong Educational Foundation for fellowship support.

References

- 1 B. C. H. Steele and A. Heinzel, *Nature*, 2001, **414**, 345–352.
- 2 S. B. Adler, *Chem. Rev.*, 2004, **104**, 4791–4843.
- 3 H. A. Gasteiger and N. M. Markovic, *Science*, 2009, **324**, 48–49.
- 4 W. Jung and H. L. Tuller, *Adv. Energy Mater.*, 2011, **1**, 1184–1191.
- 5 K. T. Lee and A. Manthiram, *J. Electrochem. Soc.*, 2005, **152**, A197–A204.
- 6 N. P. Brandon, S. Skinner and B. C. H. Steele, *Annu. Rev. Mater. Res.*, 2003, **33**, 183–213.
- 7 F. S. Baumann, J. Fleig, H. U. Habermeier and J. Maier, *Solid State Ionics*, 2006, **177**, 1071–1081.
- 8 E. D. Wachsman and K. T. Lee, *Science*, 2011, **334**, 935–939.
- 9 R. Merkle and J. Maier, *Angew. Chem., Int. Ed.*, 2008, **47**, 3874–3894.
- 10 M. M. Kuklja, E. A. Kotomin, R. Merkle, Y. A. Mastrikov and J. Maier, *Phys. Chem. Chem. Phys.*, 2013, **15**, 5443–5471.
- 11 M. T. Greiner, M. G. Helander, W. M. Tang, Z. B. Wang, J. Qiu and Z. H. Lu, *Nat. Mater.*, 2012, **11**, 76–81.
- 12 N. A. Deskins, R. Rousseau and M. Dupuis, *J. Phys. Chem. C*, 2010, **114**, 5891–5897.
- 13 J. Hayd, H. Yokokawa and E. Ivers-Tiffée, *J. Electrochem. Soc.*, 2013, **160**, F351–F359.
- 14 M. Sase, F. Hermes, K. Yashiro, K. Sato, J. Mizusaki, T. Kawada, N. Sakai and H. Yokokawa, *J. Electrochem. Soc.*, 2008, **155**, B793–B797.

- 15 M. Sase, K. Yashiro, K. Sato, J. Mizusaki, T. Kawada, N. Sakai, K. Yamaji, T. Horita and H. Yokokawa, *Solid State Ionics*, 2008, **178**, 1843–1852.
- 16 E. J. Crumlin, E. Mutoro, S. J. Ahn, G. J. la O', D. N. Leonard, A. Borisevich, M. D. Biegalski, H. M. Christen and Y. Shao-Horn, *J. Phys. Chem. Lett.*, 2010, **1**, 3149–3155.
- 17 K. Yashiro, T. Nakamura, M. Sase, F. Hermes, K. Sato, T. Kawada and J. Mizusaki, *Electrochem. Solid-State Lett.*, 2009, **12**, B135–B137.
- 18 Y. Chen, Z. Cai, Y. Kuru, W. Ma, H. L. Tuller and B. Yildiz, *Adv. Energy Mater.*, 2013, **3**, 1221–1229.
- 19 A. Kushima, D. Parfitt, A. Chroneos, B. Yildiz, J. A. Kilner and R. W. Grimes, *Phys. Chem. Chem. Phys.*, 2011, **13**, 2242–2249.
- 20 J. W. Han and B. Yildiz, *Energy Environ. Sci.*, 2012, **5**, 8598–8607.
- 21 O. I. Lebedev, J. Verbeeck, G. Van Tendeloo, O. Shapoval, A. Belenchuk, V. Moshnyaga, B. Damashcke and K. Samwer, *Phys. Rev. B: Condens. Matter Mater. Phys.*, 2002, **66**, 104421.
- 22 Z. Bi, J. H. Lee, H. Yang, Q. Jia, J. L. MacManus-Driscoll and H. Wang, *J. Appl. Phys.*, 2009, **106**, 094309.
- 23 A. P. Chen, Z. X. Bi, Q. X. Jia, J. L. MacManus-Driscoll and H. Y. Wang, *Acta Mater.*, 2013, **61**, 2783–2792.
- 24 J. Yoon, S. Cho, J. H. Kim, J. Lee, Z. X. Bi, A. Serquis, X. H. Zhang, A. Manthiram and H. Y. Wang, *Adv. Funct. Mater.*, 2009, **19**, 3868–3873.
- 25 Q. Su, D. Yoon, A. P. Chen, F. Khatkhatay, A. Manthiram and H. Y. Wang, *J. Power Sources*, 2013, **242**, 455–463.
- 26 Z. H. Cai, Y. Kuru, J. W. Han, Y. Chen and B. Yildiz, *J. Am. Chem. Soc.*, 2011, **133**, 17696–17704.
- 27 J. Januschewsky, M. Ahrens, A. Opitz, F. Kubel and J. Fleig, *Adv. Funct. Mater.*, 2009, **19**, 3151–3156.
- 28 Y. Chen, D. Fong, W. Herbert, J. P. Rueff, N. Tsvetkov and B. Yildiz, 2014, in preparation.
- 29 Y. Chen, W. Jung, Z. H. Cai, J. J. Kim, H. L. Tuller and B. Yildiz, *Energy Environ. Sci.*, 2012, **5**, 7979–7988.
- 30 H. Jalili, J. W. Han, Y. Kuru, Z. H. Cai and B. Yildiz, *J. Phys. Chem. Lett.*, 2011, **2**, 801–807.
- 31 M. Kakihana and M. Yoshimura, *Bull. Chem. Soc. Jpn.*, 1999, **72**, 1427–1443.
- 32 *NIST Database 82*, U.S. Department of Commerce, Washington, DC, 2001.
- 33 V. V. Vashook, H. Ullmann, O. P. Olshevskaya, V. P. Kulik, V. E. Lukashevich and L. V. Kokhanovskij, *Solid State Ionics*, 2000, **138**, 99–104.
- 34 A. Petric, P. Huang and F. Tietz, *Solid State Ionics*, 2000, **135**, 719–725.
- 35 R. L. Penn and J. F. Banfield, *Science*, 1998, **281**, 969–971.
- 36 M. Hawley, I. D. Raistrick, J. G. Beery and R. J. Houlton, *Science*, 1991, **251**, 1587–1589.
- 37 W. K. Burton, N. Cabrera and F. C. Frank, *Phil. Trans. Roy. Soc. Lond. Math. Phys. Sci.*, 1951, **243**, 299–358.
- 38 Y. G. Li and Y. Y. Wu, *Chem. Mater.*, 2010, **22**, 5537–5542.
- 39 S. A. Morin, M. J. Bierman, J. Tong and S. Jin, *Science*, 2010, **328**, 476–480.
- 40 F. Meng, S. A. Morin, A. Forticaux and S. Jin, *Acc. Chem. Res.*, 2013, **46**, 1616–1626.
- 41 G. J. la O', S.-J. Ahn, E. Crumlin, Y. Orikasa, M. D. Biegalski, H. M. Christen and Y. Shao-Horn, *Angew. Chem., Int. Ed.*, 2010, **49**, 5344–5347.
- 42 J. L. MacManus-Driscoll, P. Zerrer, H. Y. Wang, H. Yang, J. Yoon, A. Fouchet, R. Yu, M. G. Blamire and Q. X. Jia, *Nat. Mater.*, 2008, **7**, 314–320.
- 43 M. V. Ganduglia-Pirovano, A. Hofmann and J. Sauer, *Surf. Sci. Rep.*, 2007, **62**, 219–270.
- 44 N. Tsvetkov, Y. Chen and B. Yildiz, *J. Mater. Chem. A*, 2014, **2**, 14690–14695.
- 45 W. C. Chueh and S. M. Haile, *Annu. Rev. Chem. Biomol. Eng.*, 2012, **3**, 313–341.
- 46 J. Fleig, *Solid State Ionics*, 2002, **150**, 181–193.
- 47 W. Jung and H. L. Tuller, *J. Electrochem. Soc.*, 2008, **155**, B1194–B1201.
- 48 F. P. F. van Berkel, S. Brussel, M. van Tuel, G. Schoemakers, B. Rietveld and P. V. Aravind, *Proceedings of the 7th European Solid Oxide Fuel Cell Forum*, ed. J. A. Kilner, 2006, p. 1.
- 49 S. B. Adler, *Solid State Ionics*, 1998, **111**, 125–134.
- 50 A. Heel, P. Holtappels and T. Graule, *J. Power Sources*, 2010, **195**, 6709–6718.
- 51 C. Peters, A. Weber and E. Ivers-Tiffée, *J. Electrochem. Soc.*, 2008, **155**, B730–B737.
- 52 S. Wang, J. Yoon, G. Kim, D. Huang, H. Wang and A. J. Jacobson, *Chem. Mater.*, 2010, **22**, 776–782.
- 53 M. Kubicek, A. Limbeck, T. Fromling, H. Hutter and J. Fleig, *J. Electrochem. Soc.*, 2011, **158**, B727–B734.
- 54 Z. H. Cai, M. Kubicek, J. Fleig and B. Yildiz, *Chem. Mater.*, 2012, **24**, 1116–1127.
- 55 W. Lee, J. W. Han, Y. Chen, Z. H. Cai and B. Yildiz, *J. Am. Chem. Soc.*, 2013, **135**, 7909–7925.
- 56 P. A. W. van der Heide, *Surf. Interface Anal.*, 2002, **33**, 414–425.
- 57 J. C. Dupin, D. Gonbeau, P. Vinatier and A. Levasseur, *Phys. Chem. Chem. Phys.*, 2000, **2**, 1319–1324.
- 58 E. J. Crumlin, E. Mutoro, Z. Liu, M. E. Grass, M. D. Biegalski, Y. L. Lee, D. Morgan, H. M. Christen, H. Bluhm and Y. Shao-Horn, *Energy Environ. Sci.*, 2012, **5**, 6081–6088.